
AUTOMATED ANALYSIS OF RIPPLE-SCALE GRAVITY WAVE STRUCTURES IN THE MESOSPHERE USING CONVOLUTIONAL NEURAL NETWORKS

A PREPRINT

J. Hu¹, A. Liu¹, A. Feener¹, W. Dong¹

¹Embry-Riddle Aeronautical University, Daytona Beach, FL, USA
huj7@erau.edu

J. Li^{2,3}

²National Satellite Meteorological Center (National Center for Space Weather),
China Meteorological Administration, Key Laboratory of Space Weather, Beijing, China

³Innovation Center for Feng Yun Meteorological Satellite (FYSIC), Beijing, China

T. Li⁴

⁴University of Science and Technology of China, Hefei, China

March 5, 2026

ABSTRACT

The mesosphere and lower thermosphere (MLT), spanning approximately 80–100 km in altitude, is a region of intense dynamical activity where atmospheric gravity waves amplify due to decreasing air density. These waves often undergo breaking, inducing energy and momentum dissipation as well as turbulent mixing. These processes can be described by atmospheric instabilities—including convective and shear instabilities—that regulate the vertical coupling between atmospheric layers. Ripple-like structures observed in mesospheric airglow imagery represent small-scale, short-lived signatures of such instabilities. Their occurrence often reflects localized instabilities, critical wave interactions, or wave ducting phenomena. Therefore, detecting and analyzing these features across broad spatial and temporal domains remains a challenge. In this study, we develop a deep learning framework using convolutional neural networks (CNNs) to automatically detect ripple-scale wave structures in all-sky airglow images. Trained on labeled datasets with recognized ripples, the model learns the spatial morphology associated with instability-driven gravity waves and achieves high accuracy in identifying ripple events. Beyond detection, we perform a statistical characterization of the detected ripples to examine their frequency of occurrence, orientation distributions, scales, and geographic and seasonal variability. These statistics are used to infer underlying physical mechanisms, such as localized instability conditions and background wind filtering. This work advances our understanding of instability-driven dynamics in the upper atmosphere through AI-powered detection, while also highlighting the potential of deep learning in scientific research.

Keywords Atmospheric and Oceanic Physics · Gravity Waves · Mesosphere · Airglow Imaging · Deep Learning

1 Introduction

The mesosphere and lower thermosphere (MLT) is a dynamically active region in which atmospheric gravity waves amplify and frequently undergo breaking, generating turbulence, mixing, and vertical coupling Vincent [2015]. The turbulence associated with these instabilities contributes to the redistribution of key constituents such as O₃, atomic oxygen, and metallic species, thereby influencing the region’s radiative balance and chemical structure. Instability

processes in the MLT include both dynamical (shear-driven) instabilities, such as Kelvin–Helmholtz billows arising from strong vertical wind shear, and convective (buoyancy-driven) instabilities associated with superadiabatic lapse rates. Short-lived, small-scale “ripples” observed in OH airglow imagery represent visible manifestations of these processes Taylor and Hapgood [1990], Li et al. [2005]. Numerical simulations and coordinated lidar–radar–imager case studies suggest that ripple orientation relative to parent gravity-wave fronts and their advection characteristics may help distinguish instability mechanisms. However, observations frequently exhibit mixed signatures, and many ripple events occur under conditions that appear stable according to classical instability indices. These complexities underscore the need for large-sample statistical studies capable of linking ripple morphology with background dynamical conditions.

Previous investigations of ripple phenomena have primarily relied on case studies and manual identification of events within airglow image archives. Ripples are typically characterized by horizontal crest-to-crest spacings of 5–15 km, lifetimes of minutes to tens of minutes, and banded intensity modulations in OH emission layers. Multi-instrument statistical analyses have demonstrated that ripple occurrence exhibits clear seasonal and local-time variability and that their advection behavior is often decoupled from background winds Li et al. [2017]. While manual catalogs provide physically informed classifications, they are inherently labor-intensive, subject to observer bias, and limited in scalability when applied to multi-year datasets. Moreover, faint or borderline ripple structures may be inconsistently identified, potentially biasing climatological interpretations.

Recent advances in machine learning have enabled automated identification of atmospheric gravity waves in both ground-based airglow imagery and satellite observations. Early efforts focused on all-sky airglow imager datasets, where Lai et al. [2019] developed a two-stage framework combining a CNN classifier and a Faster R-CNN object detection model to automatically extract gravity wave patterns and compute associated parameters. Their approach demonstrated that deep convolutional feature extraction could replace manual wave identification, though strict thresholds limited detection sensitivity and primarily targeted larger-scale wavefronts. More recently, Xiao et al. [2024] applied transfer learning using an Inception V3 architecture to identify gravity waves in satellite low-light imagery from VIIRS/DNB observations. By leveraging pretrained feature extractors and augmenting limited training samples, their method achieved robust classification performance (88.2% accuracy) and highlighted the potential of transfer learning for small-sample atmospheric image datasets. At the global scale, Okui et al. [2025] developed a U-Net–based CNN for semantic segmentation of gravity waves in AIRS satellite temperature retrievals and corresponding high-resolution model outputs. Their method enables consistent wave detection across observational and model data, facilitating observation-to-model comparison while mitigating the influence of instrument noise. Collectively, these studies demonstrate that deep convolutional architectures are well suited to extracting wave-like structures embedded within noisy or spatially heterogeneous atmospheric imagery. However, most existing machine-learning applications have focused on larger-scale gravity wave signatures in satellite or airglow data, and relatively few studies have specifically addressed ripple-scale, short-lived instability structures in the mesopause region. The detection of such subtle, small-amplitude features presents additional challenges in feature representation and scale sensitivity, motivating the development of tailored CNN frameworks for ripple-scale gravity wave identification.

In this study, we develop a CNN-based framework specifically designed for ripple-scale gravity wave recognition in all-sky OH airglow images. Building upon the squeeze-and-excitation (SE) mechanism introduced by Hu et al. [2018], our architecture incorporates channel-wise attention to enhance sensitivity to subtle, ripple-scale structures embedded within spatially heterogeneous airglow backgrounds. Ripple signatures are typically characterized by low-amplitude, quasi-periodic banded intensity modulations that coexist with larger-scale gravity wave patterns and nonuniform background emissions. Standard convolutional layers treat all feature channels equally, potentially limiting the network’s ability to distinguish weak instability-driven structures from background variability. The SE block introduces adaptive channel recalibration through global context aggregation, allowing the network to emphasize feature maps that capture coherent ripple morphology while suppressing noise-dominated responses. Using this SE-enhanced CNN trained on manually annotated ripple examples, we enable automated detection of small-scale instability signatures across extensive image archives. The resulting event catalog is validated against human-identified ripples and used to construct statistical distributions of occurrence frequency, orientation, scale, and seasonal variability. By combining adaptive feature extraction with physically grounded interpretation, this work provides a scalable pathway toward long-term climatologies of mesospheric instability activity and advances the application of modern data-driven techniques in upper atmospheric research.

2 Methodology

2.1 Dataset

The airglow images used in this study were obtained from the all-sky imager located at Yucca Ridge Field Station (YRFS) in Fort Collins, Colorado (40.7°N, 104.9°W) Nakamura et al. [2005]. The imager captures the OH airglow

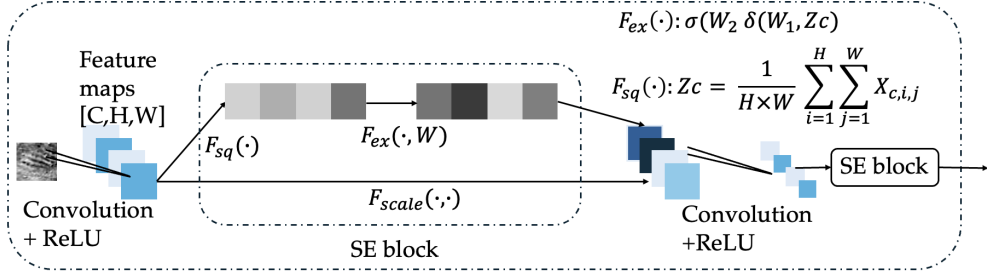


Figure 1: Schematic illustration of the squeeze-and-excitation (SE) block used in the convolutional neural network. Input feature maps of size $[C, H, W]$ are first passed through a convolutional layer followed by a ReLU activation. The squeeze operation $F_{sq}(\cdot)$ applies global average pooling over the spatial dimensions to generate channel-wise descriptors Z_c . These descriptors are then processed by the excitation operation $F_{ex}(\cdot)$, which consists of two fully connected layers with a nonlinear activation and a sigmoid function to produce channel-wise weights. The resulting weights are applied through the scaling operation $F_{scale}(\cdot)$ to recalibrate the original feature maps, which are subsequently passed to the next convolutional layer.

emission every 2 minutes, with a peaking altitude at approximately 87 km Taylor and Hill [1991]. It consists of a Nikon fish-eye Nikkor ($f = 8\text{mm}$, $f/2.8$) lens (roughly 180° field-of-view) and a CCD camera with a Kodak 1024×1024 CCD chip binned to 512×512 .

To prepare the train/test datasets, each intensity frame is normalized and clipped into the range of $[0, 1]$:

$$I_{\text{norm}}(x, y) = \text{clip} \left(\frac{I(x, y) - \text{median}(I)}{8 \text{MAD}(I)} + 0.5, 0, 1 \right) \quad (1)$$

Where

$$\text{MAD}(I) = \text{median}(|I - \text{median}(I)|) \quad (2)$$

The MAD provides a robust measure of intensity variability that is less sensitive to localized bright features (e.g., stars or instrumental artifacts) than the standard deviation. The factor of 8 was empirically selected to scale typical background variability into the $[0, 1]$ range while preserving ripple-scale contrast. Clipping suppresses extreme intensity excursions and improves numerical stability during training. Each normalized all-sky image is divided into a set of small overlapping patches. Each patch is 41×41 pixels in size, which corresponds to a roughly fixed km-scale area. Patches were centered either at known ripple locations from manual annotations of training images, or at randomly sampled background locations with no visible ripple, ensuring a balanced representation of ripple and non-ripple examples in the training data. Each patch is labeled as “ripple” or “non-ripple”. The amounts of ripple and none-ripple patch are approximately equivalent, around 1500 for both category. To enhance generalization, random horizontal and vertical flips and small rotations ($\pm 10^\circ$) were applied during training.

2.2 Neural Network Architecture

We implemented a CNN classifier augmented with a squeeze-and-excitation (SE) block (Figure 1). The SE mechanism adaptively recalibrates channel-wise feature responses through global average pooling followed by learned gating, allowing the network to emphasize feature maps that capture coherent banded ripple structures while suppressing noise-dominated or large-scale background features.

To objectively and efficiently identify gravity wave breaking signatures in large airglow image datasets, we have developed a simple CNN-based model (6 layers with 16, 32, 32, 64, 64, 128 nodes in each layer, with a fully connected layer at the end) trained using hundreds of manually identified ripple structures in a 40×40 pixel image. The convolutional feature maps after each layer are passed through an SE block and then to a fully connected layer with sigmoid activation to produce a ripple probability.

2.3 Training Strategy

The model was trained using binary cross-entropy loss and optimized with the Adam algorithm (learning rate $\eta = 10^{-3}$, weight decay 10^{-4}). Training proceeded for 30 epochs with a batch size of 64. A stepwise learning rate scheduler

reduced η by a factor of 0.5 every 10 epochs. Early stopping based on validation loss was implemented to prevent overfitting.

The dataset was partitioned into independent training (70%), validation (15%), and testing (15%) subsets. Patches derived from the same image were assigned to the same subset to prevent data leakage. All hyperparameter tuning was performed using only the training and validation sets.

Model performance on the hold-out test set was evaluated using classification accuracy, precision, recall, and F1-score. These metrics quantify overall correctness, reliability of ripple detections, completeness of ripple recovery, and the harmonic balance between precision and recall, respectively.

2.4 Full-Image Ripple Detection and Event Definition

After training, the SE-CNN model was applied to full images using a sliding-window approach with a stride of 5 pixels. Each patch was assigned a ripple probability, and patches exceeding a classification threshold of 0.5 were labeled as ripple-positive.

Spatially adjacent ripple-positive patches were grouped using connected-component labeling. Clusters separated by fewer than [insert pixel threshold] pixels were merged and counted as a single ripple occurrence at that timestamp.

To define ripple events in time, spatially overlapping clusters detected in consecutive images were grouped, accounting for ripple motion. A ripple event was therefore defined as a temporally continuous sequence of spatially coherent ripple detections occurring in approximately the same geographic region.

This procedure allows automated identification of ripple presence, approximate location, and temporal evolution across the full airglow dataset.

We trained a CNN classifier coupled with squeeze-and-excitation block on the labeled patch dataset. The squeeze-and-excitation (SE) block was incorporated to enhance the network’s ability to distinguish subtle ripple-scale structures from background variability in airglow images. Ripple patterns are characterized by faint, banded intensity modulations embedded within larger-scale wave structures and nonuniform background emissions. Standard convolutional layers treat all feature channels equally, which may limit sensitivity to weak but physically meaningful spatial signatures. The SE mechanism introduces adaptive channel-wise weighting through global context aggregation, allowing the network to recalibrate feature responses based on their relative importance. In the context of ripple detection, this enables the model to emphasize channels that capture coherent banded structures while suppressing noise-dominated or large-scale background features. By dynamically modulating feature importance, the SE block improves discrimination between true instability-driven ripple patterns and spurious intensity fluctuations, thereby enhancing detection robustness.

3 Results

The performance of the SE-CNN ripple detection framework was evaluated at both the patch and event levels and systematically compared with the manually curated ripple catalog of Li et al. (2017). An example of an all-sky image with ripple probability contour is shown in Fig. 2. At the patch level, the classifier achieved an accuracy of 92%, precision of 0.89, recall of 0.93, and F1-score of 0.91 on the independent test set, indicating strong discrimination between ripple and non-ripple image regions. The slightly higher recall relative to precision reflects a modest tendency toward enhanced sensitivity to faint ripple structures, which is desirable for climatological completeness. Event-level validation provides a physically meaningful assessment. The manual catalog contains approximately 720 ripple events over the two-year analysis period. The SE-CNN identified approximately 952 events, of which roughly 650 overlapped spatially and temporally with manual detections, yielding an event-level recall of 0.90 and precision of 0.68. The relative bias of +32% indicates that the automated approach detects substantially more events than manual inspection,

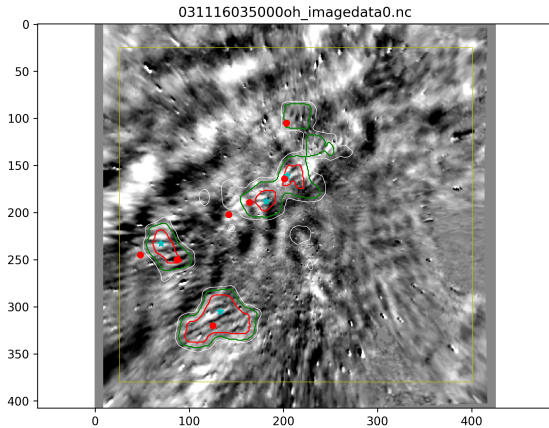


Figure 2: Example of an all-sky airglow image with several detected ripple events. The ripple structure was automatically identified by the CNN, marked by Cyan stars. The red dots are manual ripple recognitions.

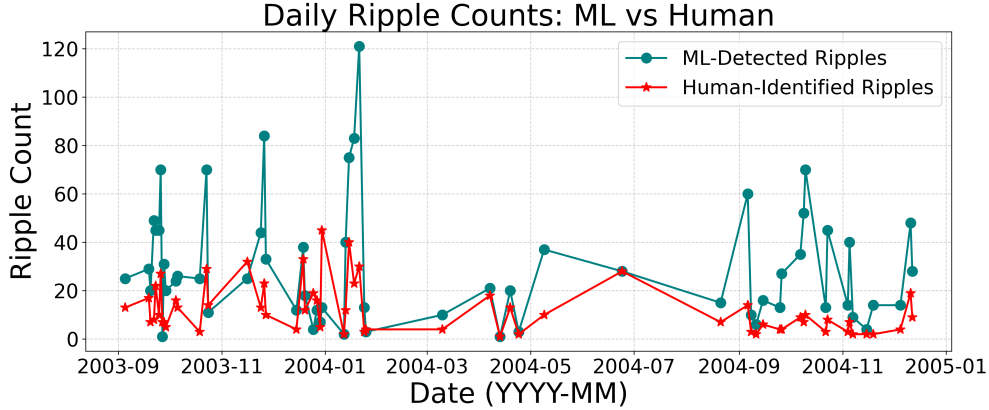


Figure 3: Distribution of ripple propagation directions for the detected events. The histogram indicates the relative frequency of ripples propagating in each azimuthal sector.

primarily due to increased sensitivity to low-amplitude, short-lived ripple signatures. Visual inspection confirms that many additional model detections correspond to weak but coherent banded structures that may fall near subjective manual thresholds.

Temporal variability is reproduced with high fidelity. Daily ripple counts derived from the SE-CNN and the manual catalog are strongly correlated (Pearson $r = 0.84$, $p < 0.001$), demonstrating that the automated framework accurately captures both active and quiescent intervals. High-activity periods during autumn 2003 and winter 2004 are consistently identified in both datasets, although peak amplitudes are larger in the automated counts due to enhanced sensitivity.

Seasonal statistics show consistent large-scale structure. Both methods identify autumn as the dominant season for ripple occurrence, with approximately 610 model detections compared to 360 manual detections. Winter activity is comparable between methods (270 model vs 280 human). Spring activity is modest (50 vs 45), while summer exhibits the lowest occurrence (22 model vs 35 human). The relative seasonal ranking (*Autumn* > *Winter* > *Spring* > *Summer*) is preserved, confirming that the automated framework reproduces the climatological modulation reported by Li et al. (2017), while systematically increasing counts during high-activity seasons. Lifetime distributions further demonstrate consistency. Indicated by Figure 6, short-lived events (0–5 min) dominate both catalogs (466 model vs 362 human) in Autumn, and the overall distribution shape is similar across seasons. The automated method identifies a slightly larger fraction of very short-lived ripples, whereas the manual catalog includes a marginally higher fraction of longer-duration events in winter. These differences likely arise from the patch-based detection framework, which emphasizes localized spatial texture and may fragment extended events into shorter segments.

Overall, across independent metrics — event recovery rate (90%), strong daily correlation ($r = 0.84$), consistent seasonal ranking, statistically similar wavelength and orientation distributions, and comparable lifetime structure — the SE-CNN framework faithfully reproduces the ripple characteristics reported by Li et al. (2017). The principal difference is increased sensitivity to faint, short-lived instability signatures, resulting in a 32% higher event count. These results demonstrate that the automated detection system is not only consistent with established manual analysis but also provides a more objective and scalable tool for constructing long-term climatologies of mesospheric instability activity.

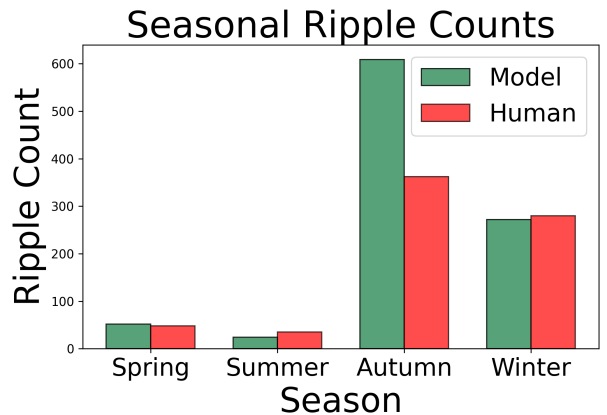


Figure 4: Seasonal variation of ripple occurrence frequency. The plot shows the mean number of ripple events detected in each season of the year.

4 Discussion

The automated SE-CNN detection framework demonstrates strong quantitative agreement with the manually curated ripple catalog of Li et al. (2017). Event-level recall of approximately 90% indicates that the vast majority of manually identified ripple events are successfully recovered by the model. Daily ripple counts are highly correlated ($r = 0.84$, $p < 0.001$), confirming that the automated system preserves the temporal structure of ripple activity, including both high-activity and quiescent intervals. Moreover, key morphological characteristics — including horizontal wavelength (5–15 km with a peak near 8–10 km), broad orientation distribution, and short-dominated lifetime structure — closely match previously reported statistics. These results collectively indicate that the SE-CNN framework faithfully reproduces the principal observational properties established in earlier manual analyses.

Despite this strong agreement, systematic differences are evident. The automated method identifies approximately 32% more ripple events than the manual catalog, with the largest discrepancy occurring during high-activity autumn periods. Examination of lifetime distributions shows that the model detects a higher fraction of very short-lived (0–5 minute) events, suggesting increased sensitivity to faint or marginal instability signatures that may fall below subjective manual detection thresholds. Conversely, slightly fewer long-duration events are identified by the automated method, likely reflecting the patch-based classification framework, which emphasizes localized spatial texture and may fragment

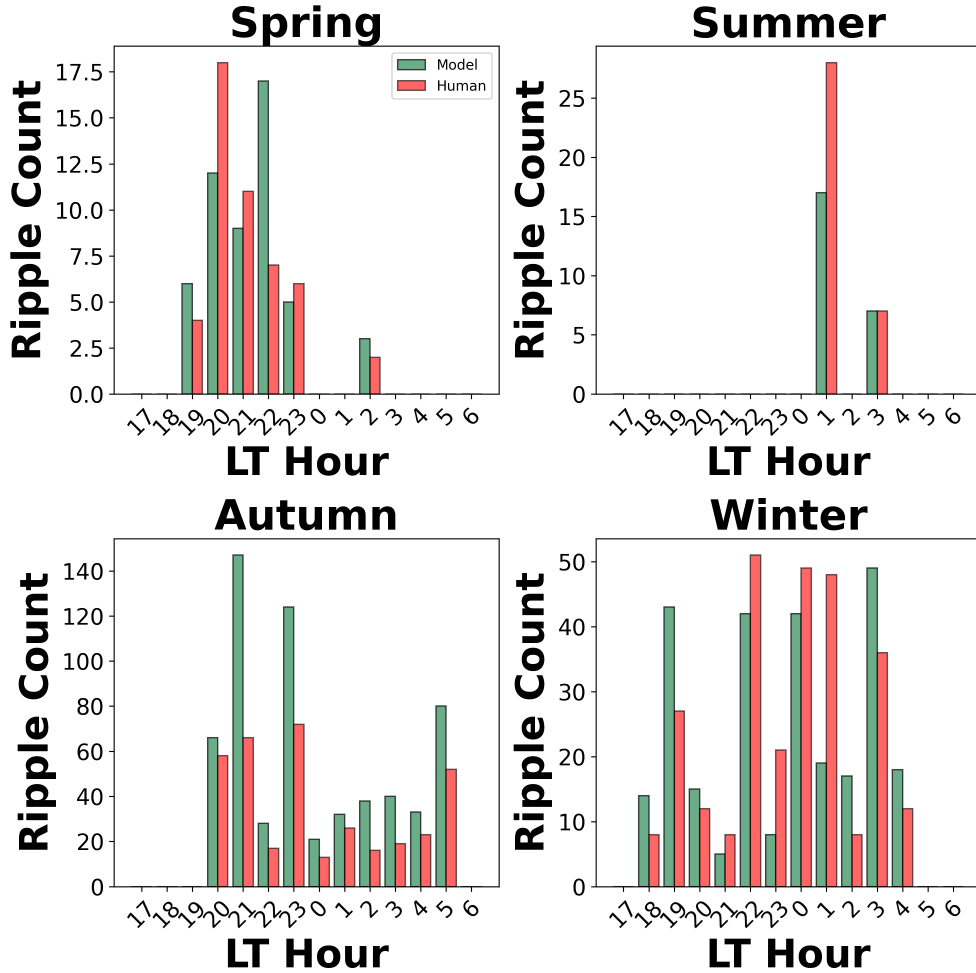


Figure 5: Seasonal distribution of ripple occurrence as a function of local time (LT) hour for spring, summer, autumn, and winter. Bars show the number of detected ripple events in each LT bin, with green representing model detections and red representing human-identified events. The comparison highlights seasonal differences in the diurnal timing of ripple occurrence and the level of agreement between the model and human observations.

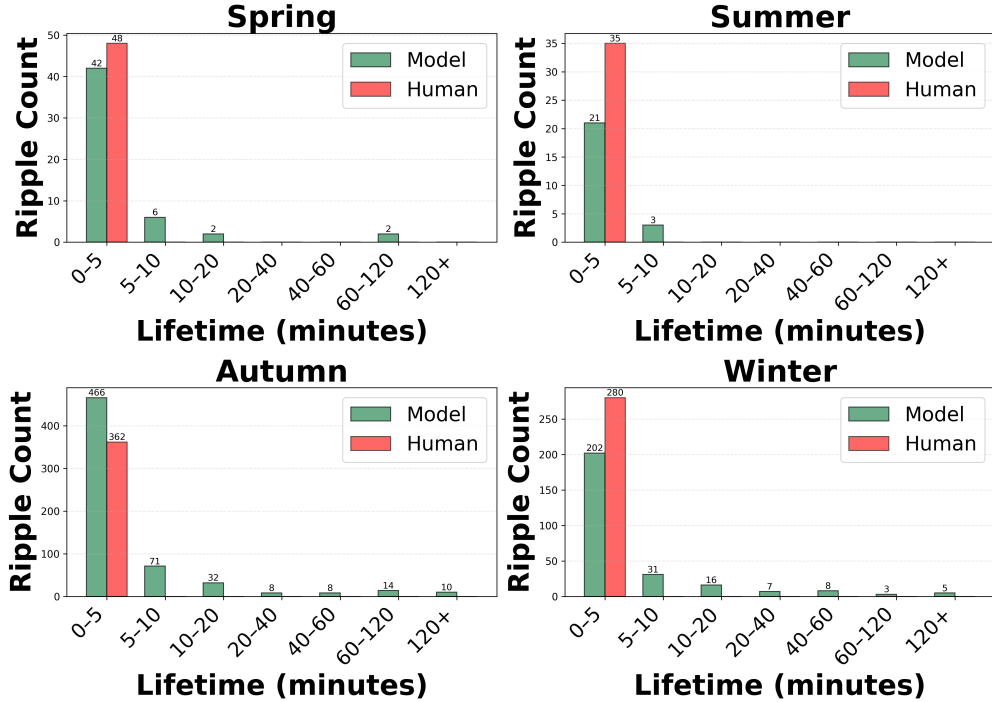


Figure 6: Seasonal distribution of ripple lifetimes for spring, summer, autumn, and winter. Ripple counts are shown for different lifetime bins (in minutes), with green bars indicating model detections and red bars indicating human-identified events. The results illustrate the dominance of short-lived ripples across all seasons, as well as differences between the model and human classifications, particularly for longer-duration events.

temporally extended events into shorter segments. These differences are physically interpretable and do not alter the overall seasonal or morphological patterns.

The seasonal modulation reproduced by the automated detections provides further physical validation. Both methods indicate enhanced ripple occurrence during autumn and winter relative to summer, consistent with stronger background wind shear and dynamical instability conditions during these seasons at mid-latitudes. The pronounced autumn maximum likely reflects favorable filtering of gravity waves and enhanced mesospheric shear associated with seasonal circulation transitions. The broad distribution of ripple propagation directions further supports the interpretation that ripple formation is governed primarily by local instability conditions rather than preferred gravity-wave source direction. The absence of a dominant orientation aligns with the conclusion of Li et al. (2017) that ripple occurrence is not strongly constrained by large-scale wave propagation direction.

Importantly, the automated approach offers methodological advantages beyond simple replication of manual results. First, it removes observer-dependent variability by applying a consistent decision boundary across the entire dataset. Second, it enhances sensitivity to low-amplitude ripple signatures, potentially revealing instability activity that is underrepresented in manually curated catalogs. Third, the computational efficiency of the SE-CNN framework enables rapid processing of extended multi-year archives, making construction of long-term ripple climatologies feasible. Such scalability is essential for investigating interannual variability, coupling with meteor radar wind measurements, and potential climate-scale trends in mesospheric instability occurrence.

Several limitations warrant consideration. The classifier is trained on manually labeled examples from a specific site, and its performance may depend on the representativeness of the training data. Imaging conditions such as auroral contamination, cloud interference, or extremely faint ripple structures may reduce detection reliability. In addition, the patch-based detection and clustering approach provides event occurrence and approximate location but does not directly yield high-precision geometric measurements of ripple amplitude or wavelength. Future work could integrate object-detection or segmentation frameworks to improve spatial delineation of ripple fronts and enable automated extraction of quantitative wave parameters.

Overall, the strong agreement across multiple independent validation metrics — including event recovery rate, temporal correlation, seasonal modulation, and morphological consistency — demonstrates that the SE-CNN framework provides

a reliable and objective surrogate for manual ripple identification. The enhanced sensitivity and scalability of the automated approach establish a robust foundation for comprehensive, long-term studies of mesospheric gravity wave instability dynamics.

References

- Robert A Vincent. The dynamics of the mesosphere and lower thermosphere: A brief review. *Progress in Earth and Planetary Science*, 2(1):4, 2015.
- Michael J Taylor and MA Hapgood. On the origin of ripple-type wave structure in the oh nightglow emission. *Planetary and space science*, 38(11):1421–1430, 1990.
- Tao Li, CY She, Bifford P Williams, Tao Yuan, Richard L Collins, Lois M Kieffaber, and Alan W Peterson. Concurrent oh imager and sodium temperature/wind lidar observation of localized ripples over northern colorado. *Journal of Geophysical Research: Atmospheres*, 110(D13), 2005.
- Jing Li, Tao Li, Xiankang Dou, Xin Fang, Bing Cao, Chiao-Yao She, Takuji Nakamura, Alan Manson, Chris Meek, and Denise Thorsen. Characteristics of ripple structures revealed in oh airglow images. *Journal of Geophysical Research: Space Physics*, 122(3):3748–3759, 2017.
- Chang Lai, Jiyao Xu, Jia Yue, Wei Yuan, Xiao Liu, Wei Li, and Qinzeng Li. Automatic extraction of gravity waves from all-sky airglow image based on machine learning. *Remote Sensing*, 11(13):1516, 2019.
- Beimin Xiao, Shensen Hu, Weihua Ai, and Yi Li. Atmospheric gravity wave detection in low-light images: A transfer learning approach. *Electronics*, 13:4030, 2024.
- Haruka Okui, Corwin J. Wright, Peter G. Berthelemy, Neil P. Hindley, Lars Hoffmann, and Andrew P. Barnes. A convolutional neural network for the detection of gravity waves in satellite observations and numerical simulations. *Geophysical Research Letters*, 52:e2025GL115683, 2025.
- Jie Hu, Li Shen, and Gang Sun. Squeeze-and-excitation networks. In *Proceedings of the IEEE conference on computer vision and pattern recognition*, pages 7132–7141, 2018.
- T Nakamura, T Fukushima, T Tsuda, C-Y She, BP Williams, D Krueger, and W Lyons. Simultaneous observation of dual-site airglow imagers and a sodium temperature-wind lidar, and effect of atmospheric stability on the airglow structure. *Advances in Space Research*, 35(11):1957–1963, 2005.
- Michael J Taylor and MJ Hill. Near infrared imaging of hydroxyl wave structure over an ocean site at low latitudes. *Geophysical Research Letters*, 18(7):1333–1336, 1991.